Polymer Chemistry

PAPER

Poly(ionic liquid)s-based nanocomposite polyelectrolytes with tunable ionic conductivity prepared *via* SI-ATRP†

Ping Wang,[a] Yin-Ning Zhou,[b] Jiang-Shui Luo[c] and Zheng-Hong Luo*[b]

In this study, a novel kind of organic−inorganic core−shell SiO$_2$-poly(p-vinylbenzyl) trimethylammonium tetrafluoroborate (SiO$_2$−P[VBTMA][BF$_4$]) nanoparticle was well designed and successfully synthesized *via* surface-initiated atom transfer radical polymerization (SI-ATRP). Fourier transform infrared spectroscopy (FT-IR), ^{1}H nuclear magnetic resonance (^{1}H NMR), X-ray photoelectron spectroscopy (XPS), dynamic light scattering (DLS) and scanning electron microscopy (SEM) were used to confirm the formation of the core−shell nanoparticles and the surface modification. In order to overcome the challenge of the characterization of the number average molecular weight of poly(ionic liquid)s, "sacrificial initiator" method was used here employing a trimethylsilyl (TMS)-labeled initiator as the NMR marker for integration. In addition, good thermal stability of the new hybrid polyelectrolyte was proved by thermogravimetric analysis. The electrochemical impedance measurements revealed that the room temperature conductivity reached 10^{-4} S cm^{-1}, which is much higher than that of the pure poly(ionic liquid)s and varies with the amount of the grafted polymer and the test temperature. The X-ray diffraction (XRD) tests further investigated the crystal structure of the nanocomposite and pure P[VBTMA][BF$_4$]. The temperature dependence of ionic conductivity conforms to Arrhenius behavior for both of the nanocomposites and the pure polymer. The results indicated that the SI-ATRP approach provided a simple and versatile route to tune the ionic conductivity of the hybrid nanoparticles by changing the chain length of the grafted polymer, which can be potentially used in a variety of electrochemical devices.

1. Introduction

Ion-conducting materials are important components in a variety of energy conversion devices, such as all-solid-state lithium-metal–polymer batteries, fuel cells, dye-sensitized solar cells, light-emitting electrochemical cells, and other electrochemical devices.[1,2] Poly(ionic liquid)s as one type of polymer electrolyte, which improve the stability of ionic liquids by tethering ion conducting groups to the polymer backbone, were found to play an enabling role in some fields of polymer chemistry and materials science.[3–6] Studies of poly(ionic liquid)s have been overwhelmingly concentrated on the introduction of polymerizable groups to the ionic liquid cations, where the common groups are acryloyl or vinyl. However, the polymerization of ionic compounds inevitably reduces the ion motion and thus the resulting ionic conductivity at ambient temperature is relatively too low for commercial applications. Much work has been carried out to optimize the polymer electrolytes to enhance their ionic conductivity, thermal stability, and electrochemical stability as the prerequisite for their use in lithium rechargeable batteries at ambient temperature.[7–10] For example, the formation of well-defined polymer/inorganic nanoparticle hybrid materials are critical to the development of nanomaterials with desired optical, electric, magnetic, mechanical, and electrochemical properties.[11–18] Various nanoscale cores, including montmorillonite, gold, CdSe, aluminum oxide and silica, have been reported.[14–16,19] Nanosilica, one of the most common spherical nanoscale particles, is chemically inert but allows irreversible surface modification by reaction of the surface silanol groups.[19,20] Due to the nanoscale effects, polymer/silica nanocomposites can often exhibit dramatic improvements in strength, modulus, heat resistance, gas permeability barrier properties and so on.[21,22] What is more, the addition of the non-conducting filler produces an increase in the conductivity of both semi-crystalline and amorphous polymer electrolytes.[23–27] Therefore, by incorporating poly(ionic liquid)s onto inorganic nanoparticles to form core–shell structures, it is possible to provide complementary functionality (*i.e.*, structural stability) and transport tunability to ion-conducting materials.

[a]Department of Chemical and Biochemical Engineering, College of Chemistry and Chemical Engineering, Xiamen University, Xiamen 361005, P. R. China

[b]Department of Chemical Engineering, School of Chemistry and Chemical Engineering, Shanghai Jiao Tong University, Shanghai 200240, P. R. China. E-mail: luozh@sjtu.edu.cn; Fax: +86-21-54745602; Tel: +86-21-54745602

[c]Department of Metallurgy and Materials Engineering, KU Leuven, Kasteelpark Arenberg 44 - box 2450, 3001 Leuven, Belgium

† Electronic supplementary information (ESI) available. See DOI: 10.1039/c3py01025b

Hybrid nanoparticles can be prepared by either physical adsorption or covalent grafting techniques including "grafting to" and "grafting from" methods. Because of its high tethering density, the "grafting from" method is more attractive. Controlled/"living" radical polymerizations, such as atom transfer radical polymerization (ATRP), have been shown to give very satisfactory results because of their high tethering density by the "grafting from" method.[28–31] It has been widely studied for planar surfaces,[32–40] and some work on spherical particles has also been reported.[41–45] Surface initiated-ATRP (SI-ATRP) on nanosilica particles was first reported by Patten *et al.*, who discovered that it provides a good strategy for formation of core–shell microspheres with a controllable shell layer.[46]

As a kind of hydrophilic ionic liquid monomer, (*p*-vinylbenzyl) trimethylammonium tetrafluoroborate ([VBTMA][BF$_4$]) was chosen due to its ion-conducting system for applications that involve exposure to air and inevitable contact with water vapor. The presence of water is anticipated to have a strong effect on transport properties of the nanocomposites as it can be absorbed by the hydrophilic poly(*p*-vinylbenzyl) trimethylammonium tetrafluoroborate (P[VBTMA][BF$_4$]) shell, and thus increases the volume fraction of the conducting phase allowing for greater mobility of P[VBTMA][BF$_4$] polymer chains, resulting in enhanced ionic conductivity.[22,27]

Therefore, we try to synthesize a novel kind of organic–inorganic nanoparticle with a core–shell structure which combines the strength properties and the ion-conducting properties with a synergistic effect. Firstly, [VBTMA][BF$_4$] monomers were grafted onto the nanosilica particles, which have a small size, high specific surface area and provided as a rigid support, by SI-ATRP. The trimethylsilyl (TMS)-labeled "sacrificial initiator" method[33,47–50] was applied to trace the polymerization and characterize the molecular weight of poly(ionic liquid)s. In addition, the ionic conductivity and ion conduction mechanism of the nanocomposites were investigated initially. Such an insight into the fundamental structure–property relationship which governs ion conduction is critical for developing next generation of ion-conducting materials.

2. Experimental

2.1 Materials

Nanosilica (with an average particle size of 14 nm and a specific surface area of 200 ± 25 m^2 g^{-1}), (*p*-vinylbenzyl)trimethylammonium chloride ([VBTMA][Cl], 99%), deuterated chloroform (CDCl$_3$, 99.9%), deuterated dimethylsulfoxide-d_6 (DMSO-d_6, 99.9%), and 1,1,4,7,7-pentamethyldiethylenetriamine (PMDETA, 98%) were purchased from Sigma Aldrich. Nanosilica was preheated at 110 °C under vacuum overnight. 3-Aminopropyltriethoxysilane (APTES, 98%) was bought from Alfa Aesar. 2-Bromoisobutyryl bromide (BiBB, 98%) was obtained from A Better Choice for Research Chemicals GmbH & Co. KG (ABCR). Sodium tetrafluoroborate (NaBF$_4$, 99%) and 2-(trimethylsilyl)ethanol (99%) were purchased from Aladdin. CuCl (99%, Sinopharm Chemical Reagent Co., Ltd (SCRC)) was purified by washing it with acetic acid and methanol alternatively three times and then dried under vacuum at 45 °C for

24 h. All other chemicals were obtained from SCRC and used without further purification.

2.2 Synthesis of amino-functionalized silica nanoparticles (SiO$_2$–NH$_2$)

Functionalization of nanosilica by converting most of the surface silanol groups into amino groups was carried out as follows. The silica dispersion (2.00 g SiO$_2$, 2 wt% in toluene) was transferred into a 250 mL 2-neck round-bottom flask and then put it on a magnetic stirrer fitted with a reflux condenser. APTES (4.38 mL, 18.72 mmol) was added, pumped and vacuum-purged with nitrogen gas three times. Then the reaction mixture was gently refluxed overnight under nitrogen. After cooling to room temperature, the nanoparticles were isolated by centrifugation at 4000 rpm for 10 min. After discarding the supernatant, the sediments were crushed and redispersed in toluene and centrifuged again. The centrifugation–redispersion cycle was repeated twice using dichloromethane and acetone, separately. The functionalized silica was dried in vacuum at 45 °C for 24 h and then stored in a silica gel desiccator. The amount of amino groups introduced onto the silica surface was determined by elemental analysis. The results of the elemental analysis of the same sample, which was tested twice under the same conditions, are shown in Table 1. Since there is only one N atom in each APTES molecule, the graft density of amino (D_{NH_2}) is also the graft density of APTES, which can be calculated by eq (1):

$$D_{NH_2} = \frac{C_N}{M_N} \qquad (1)$$

wherein C_N is the N content according to the elemental analysis, and M_N is the molecular weight of the N atom. As a result, the graft density of APTES is calculated to be 1.64 mmol g^{-1}.

2.3 Synthesis of the silica macroinitiator (SiO$_2$–Br)

To carry out the SI-ATRP of the ionic liquid, the initiator was first grafted onto the SiO$_2$ particles. The toluene suspension of amino-functionalized silica nanoparticles (1.5 g SiO$_2$–NH$_2$, 2 wt% in toluene) was mixed with triethylamine (1.71 mL, 12.3 mmol) in a 150 mL flask. After cooling to 0 °C, BiBB (0.61 mL, 4.92 mmol) was added dropwise. The solution was stirred at 0 °C for 2 h and then at room temperature for another 22 h. The nanoparticles were purified and isolated following similar procedures for the synthesis of amino-functionalized silica nanoparticles described in Section 2.2. The final product was dried in a vacuum oven at 45 °C for 24 h.

Table 1 Repeated elemental analysis of SiO$_2$-APTES

No.	Weight (mg)	Content [N] (%)	Content [C] (%)	Content [H] (%)	C/N ratio
1	5.160	2.296	6.301	1.991	2.744
2	4.520	2.302	6.136	1.852	2.665

2.4 Synthesis of the TMS-labeled ATRP initiator

2-(Trimethylsilyl)ethanol (1.419 g, 12.0 mmol), anhydrous CH_2Cl_2 (10 mL), and triethylamine (1.95 mL, 14.0 mol) were added into a 60 mL round-bottom flask equipped with a rubber plug. After the flask was immersed into an ice-water bath, BiBB (1.73 mL, 14.0 mmol) in anhydrous CH_2Cl_2 (5 mL) was added dropwise into the previous solution. The reaction was continued at 0 °C for another 2 h and then at room temperature for 24 h. The reaction mixture was then filtered to remove the salt, and then washed successively with 1 mol L^{-1} HCl solution, 1 mol L^{-1} $NaHCO_3$ solution, and deionized water. The organic phase was dried with anhydrous $MgSO_4$ overnight. After filtration and removal of dichloromethane on a rotary evaporator, a faint yellow viscous liquid of 2-(trimethylsilyl)ethyl 2-bromo-2-methylpropanoate (TMS-EBMP) was obtained. ^{1}H NMR (400 MHz, $CDCl_3$) δ (ppm): 4.30 (t, 2H), 1.94 (s, 6H), 1.05 (s, 2H), 0.08 (t, 9H).

2.5 Synthesis of the ionic liquid monomer [VBTMA][BF₄]

The monomer was synthesized from ammonium halide using ion exchange reaction as follows: [VBTMA][Cl] (2.54 g, 0.012 mol), $NaBF_4$ (1.45 g, 0.0132 mol) and acetonitrile (CH_3CN) (15 mL) were added to a 60 mL round-bottom flask. The mixture was stirred overnight. The salt dissolved gradually and finally formed a white precipitate. The precipitate was removed by filtration. The filtrate was concentrated, and then poured into ether. The precipitated white crystal was collected and dried under vacuum at room temperature and stored in a refrigerator. In addition, silver nitrate testing indicated the absence of chloride. [VBTMA][BF₄]: ^{1}H NMR (400 MHz, DMSO-d_6) δ (ppm): 7.62 (d, 2H), 7.51 (d, 2H), 6.81 (q, 1H), 5.96 (d, 1H), 5.38 (d, 1H), 4.50 (s, 2H), 3.02 (s, 9H); mp: 160–164 °C.

2.6 Synthesis of SiO₂–P[VBTMA][BF₄] nanoparticles

The initiator-immobilized silica particles, the ionic liquid monomer [VBTMA][BF₄] (2.634 g, 10.0 mmol), dimethylformamide (DMF) (4.0 mL), and CuCl (0.0099 g, 0.1 mmol) were added in sequence into a 25 mL dry 3-neck flask, and then sealed with a rubber septum rapidly. The flask was degassed by purging with nitrogen for 10 min. TMS-labeled free initiator TMS-EBMP (13.36 mg, 0.05 mmol) was added to the mixture *via* a syringe, and the solution was stirred for about 10 min until it became homogeneous, followed by the addition of the ligand (PMDETA, 20.8 μL, 0.1 mmol) *via* a syringe to start the surface-initiated polymerization. After a desired reaction time at 90 °C, the SiO_2–P[VBTMA][BF₄] particles were isolated by centrifugation. To remove physically absorbed polymer chains, the SiO_2–P-[VBTMA][BF₄] particles were washed with DMF several times and then dried under vacuum at 70 °C. The supernatant was concentrated, and then precipitated in a cold methanol–water (4/1 v/v) mixture. The polymer (P[VBTMA][BF₄]) generated in the solution by the sacrificial initiator was obtained and dried under vacuum at 45 °C. Then the samples were kept in a desiccator for ^{1}H NMR measurement. P[VBTMA][BF₄]: ^{1}H NMR (400 MHz, DMSO-d_6) δ (ppm): 7.09 (br, 2H), 6.46 (br, 2H), 4.30 (br, 2H), 2.88 (br, 9H), 1.50 (br, 3H). Elemental analysis:

calculated for $C_{12}H_{18}NBF_4$: C, 54.75; H, 6.84; N, 5.32. Found: C, 50.78; H, 7.00; N, 5.05.

2.7 Characterizations

[1]H nuclear magnetic resonance (^{1}H NMR) spectra were recorded on a Bruker Advance II 400 MHz NMR spectrometer operated at 400 MHz in 5 mm tubes using $CDCl_3$ or DMSO-d_6 as the solvent.

Fourier transform infrared spectra (FT-IR) of the bare-silica, SiO_2–Br and SiO_2–P[VBTMA][BF₄] were recorded using KBr pellets in transmittance mode between 4000 and 400 cm^{-1} on a Nicolet Avatar 330 FT-IR spectrophotometer.

The melting point of the monomer [VBTMA][BF₄] was measured by an X-4 digital display microscopic melting point meter corrected using acetanilide with a melting point of 114 °C as the standard substance.

Thermogravimetric analysis (TGA) was carried out on an SDTQ 600 instrument at a heating rate of 10 °C min^{-1} from room temperature to 800 °C under a nitrogen atmosphere.

Elemental analysis was done using a Vario EL III elemental analyzer.

Scanning electron microscopy (SEM) observation was made using a Hitachi S-4800 microscope at an acceleration voltage of 10 kV. Each sample was prepared as follows: 0.2 mg mL^{-1} ethanol solution of bare-silica and SiO_2–Br, and 0.2 mg mL^{-1} DMF solution of P[VBTMA][BF₄] and SiO_2–P[VBTMA][BF₄] were mounted onto silicon wafers, dried at room temperature, pasted onto conducting resins, and then tested after spraying with platinum.

X-ray photoelectron spectroscopy (XPS) analysis was carried out on a PHI quantum 2000 scanning ESCA microprobe, using an Al $K_{\alpha 12}$ radiation as the exciting source with a binding energy of 1486.60 eV and voltage of 15 kV in a CAE pattern. The binding energy of carbon (C1s = 284.8 eV) was used as the energy calibration standard.

Dynamic light scattering (DLS) tested on a Malvern light scattering instrument (Nano ZS, Particle Sizing Systems) was used to measure the particle size of the nanoparticles. All hydrodynamic diameters in the text are the averages of the intensity-weighted distributions at 20 °C. The samples were prepared in DMF and filtered with a 0.45 μm nylon syringe filter.

Electrochemical impedance spectroscopy was used to measure the ionic conductivity of the materials. The impedance spectra were recorded on a CHI660D electrochemical workstation at room temperature and in the temperature range of 303.15–353.15 K. The samples were made into wafers beforehand, and sandwiched between a pair of stainless steel blocking electrodes and placed in a temperature controlled furnace to be maintained at various constant temperatures for at least 1 h prior to each measurement. The data were collected over a frequency range of $1–10^6$ Hz with an amplitude of 5 mV for an open circuit potential at different temperatures. The thickness and the diameter of the samples were measured by a vernier caliper. The bulk resistance is obtained from the Nyquist plots. The conductivity is calculated according to the following equation:

$$\sigma = \frac{L}{RS} \tag{2}$$

where L is the thickness of the composite wafer, S is the area of the composite wafer and R is the bulk resistance.

The X-ray diffraction (XRD) patterns were recorded on an X'pert PRO X-ray diffractometer operating in normal transmission mode using Cu Kα radiation ($\lambda = 1.5406$ Å).

3.   Results and discussion

3.1   Characterization of the SiO$_2$–P[VBTMA][BF$_4$] nanocomposites

Core–shell SiO$_2$–P[VBTMA][BF$_4$] was prepared *via* SI-ATRP on the macroinitiator surface (see Scheme 1). The FT-IR spectra of the silica particles, SiO$_2$–Br, and SiO$_2$–P[VBTMA][BF$_4$] are shown in Fig. 1. For bare silica (Fig. 1(a)), the characteristic absorption peaks of the tetrahedral silica structures occur at 1110 cm^{-1} (Si–O stretching) and 474 cm^{-1} (Si–O bending). A Si–O–Si bending peak at 808 cm^{-1} is observed. In the spectrum of SiO$_2$–Br (Fig. 1(b)), a small peak at 1538 cm^{-1} (N–H bending) is observed, indicating the existence of the amide group. Peaks at 2930 cm^{-1} and 1383 cm^{-1}, arising from the C–H stretching and bending vibration of the initiator, can also be observed. In the spectrum of SiO$_2$–P[VBTMA][BF$_4$] (Fig. 1(c)), the characteristic peaks of both SiO$_2$ and the polymer shell are included. The peaks at 857 cm^{-1}, 891 cm^{-1} and 920 cm^{-1}, attributed to the C–H bending vibration, along with the two sharp peaks at 1490 cm^{-1} and 1419 cm^{-1} are the characteristic peaks of the benzene ring in P[VBTMA][BF$_4$], indicating that P[VBTMA][BF$_4$] was successfully grafted onto the surface of the nanosilica particles. The ^{1}H NMR spectrum of [VBTMA][BF$_4$] in Fig. 2(a) shows the appearance of two sharp doublets at 7.62 ppm and 7.51 ppm, corresponding to protons on the benzene ring group. One
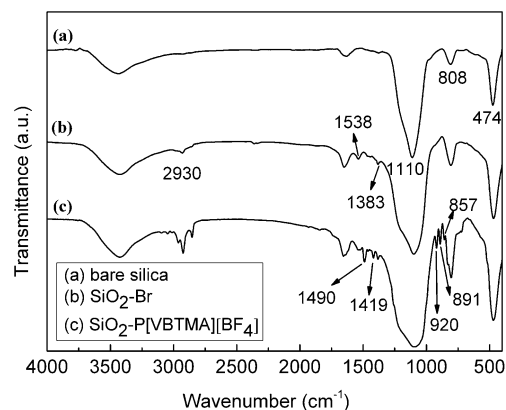

Fig. 1   FT-IR spectra of (a) bare silica, (b) SiO$_2$–Br and (c) SiO$_2$–P[VBTMA][BF$_4$].

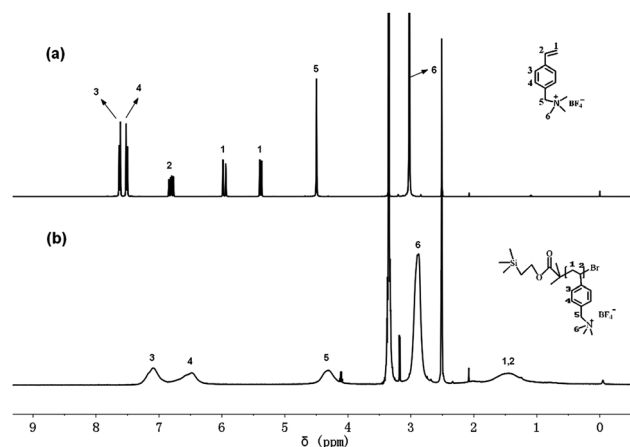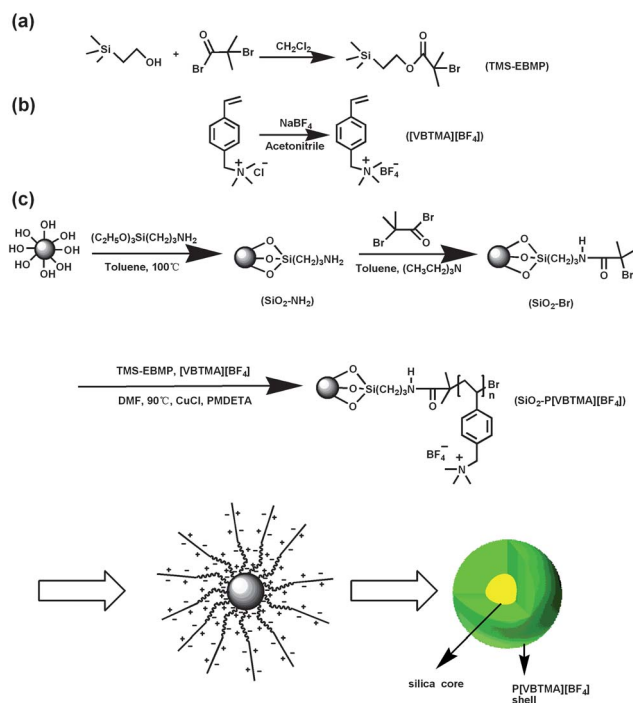Fig. 2 ^{1}H NMR spectra of (a) [VBTMA][BF$_4$] and (b) P[VBTMA][BF$_4$].

quartet centered at 6.81 ppm, and two doublets at 5.96 ppm and 5.38 ppm, corresponding to the protons attached to carbons of the C=C double bond on the styrene group, can also be observed. One singlet at 4.50 ppm corresponds to the protons on methylene which is connected to the benzene ring. Another singlet at 3.02 ppm corresponds to the protons on the methyl group connected to the nitrogen atom, and the singlet at 2.50 ppm is attributed to the solvent DMSO-d_6. One broad peak at around 1.50 ppm of P[VBTMA][BF$_4$] shown in Fig. 2(b), along with the disappearance of the peaks of the protons on the vinyl group, shows that P[VBTMA][BF$_4$] was successfully synthesized.

To further confirm the immobilization of the initiator and P[VBTMA][BF$_4$] on the surface of silica, the surface of modified silica was characterized by XPS. The XPS survey spectrum and high resolution elemental scan of C1s, N1s, and Br3d recorded from the macroinitiator SiO$_2$–Br surface as shown in Fig. 3 confirm the structure. The C1s core-level spectrum of the macroinitiator surface includes three peak components having binding energy at about 284.3 eV, 287.0 eV, and 287.8 eV, attributable to the C–H/C–C, C–Br/C–NCO, and O=C–N species, respectively. The N1s peak at the binding energy of about 402.1 eV is attributed to the O=C–N species. The presence of the Br3d
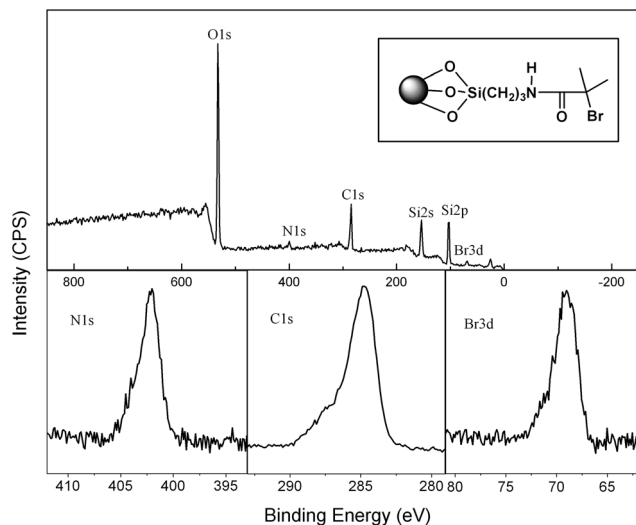

Scheme 1   Synthesis route of the "core–shell" nanocomposites.

Fig. 3 The XPS survey spectrum and high-resolution elemental scan of C1s, N1s, and Br3d of the macroinitiator SiO$_2$−Br surface.
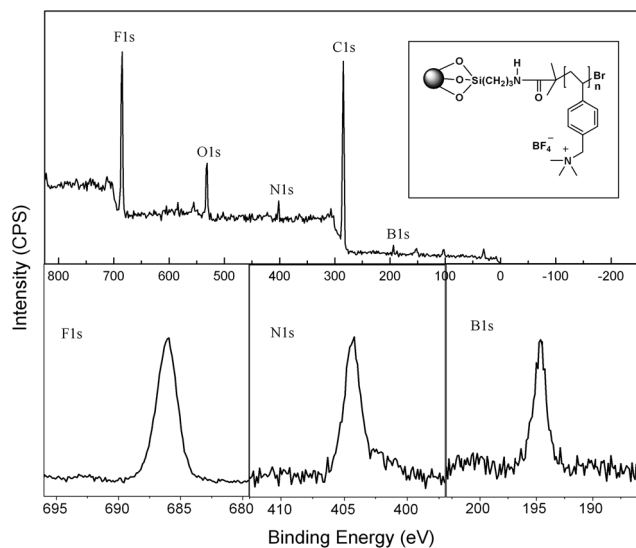

Fig. 4 The XPS survey spectrum and high-resolution elemental scan of F1s, B1s, and N1s of the SiO$_2$−P[VBTMA][BF$_4$] surface.

peak at the binding energy of about 68.7 eV and the appearance of the O=C–N peak component indicate that the initiator species for the subsequent SI-ATRP reaction has been successfully immobilized on the nanosilica surface via silanization and acylation reaction. Fig. 4 shows the typical XPS survey spectrum and high-resolution elemental scan of F1s, B1s, and N1s of the P[VBTMA][BF$_4$] shell modified silica surface. The peaks for F1s (686.1 eV), B1s (194.6 eV), and N1s (404.2 eV) are clearly seen in the survey spectrum. The N1s peak at the binding energy of 404.2 eV is mainly assigned to the positively charged nitrogen (N$^+$) of the poly[(p-vinylbenzyl)trimethylammonium] cation. By calculating the peak area of each element, the [N] : [F] : [B] ratio for the P[VBTMA][BF$_4$] shell modified silica surface was about 1.16 : 3.62 : 1, which was in good agreement with the theoretical molar ratio of those atoms (1 : 4 : 1).

In principle, the hydrodynamic diameter should increase upon complex formation as different amounts of [VBTMA][BF$_4$] are grafted onto the nanosilica particles. Therefore, we try to employ DLS to obtain the hydrodynamic diameter of the hybrid nanoparticles in solution. The approximate linearity of the particle size vs. polymerization time is observed as shown in Fig. S1.†

3.2 Molecular weight measurement

The characterization of well-defined poly-ionic materials remains a challenge for the presence of charged groups resulting in complicated and unreliable molecular weight (MW) characterization via gel permeation chromatography (GPC). He et al. demonstrated that the MW and molecular weight distribution (MWD) of poly(ionic liquid)s can be characterized by simply adding salts containing the same anions as the poly(ionic liquid)s into the GPC eluents.[50] However, this leads to complicated post-processing of the data and it is not universal for all the poly(ionic liquid)s. Therefore, the molecular weight of the polymer that was grafted onto the nanosilica was measured with a TMS-labeled "sacrificial initiator" method by ^{1}H NMR.[50–52] The ^{1}H NMR spectra of TMS-P[VBTMA][BF$_4$] at different polymerization times are shown in Fig. 5. The number average molecular weight of the precipitated TMS-P[VBTMA][BF$_4$] obtained from ^{1}H NMR ($M_{n,NMR}$) was calculated via eq (3):

$$M_{n,NMR} = \frac{9A_{benzene}M_{monomer}}{4A_{TMS}} + M_{initiator} \tag{3}$$

where $A_{benzene}$ is the integrated area of the NMR peaks (∼7.09 and 6.46 ppm) of the H in the benzene rings, A_{TMS} is the integrated area of the NMR peak (∼0.0 ppm) of the H in TMS groups, $M_{monomer}$ is the molecular weight of the [VBTMA][BF$_4$] monomer, and $M_{initiator}$ is the molecular weight of the TMS-labeled initiator.

The calculated molecular weight increases with polymerization time as shown in Fig. 6. But it is regrettable that we could not get the MWD of P[VBTMA][BF$_4$] through this method. Although there are a few reports showing that MALDI-TOF MS
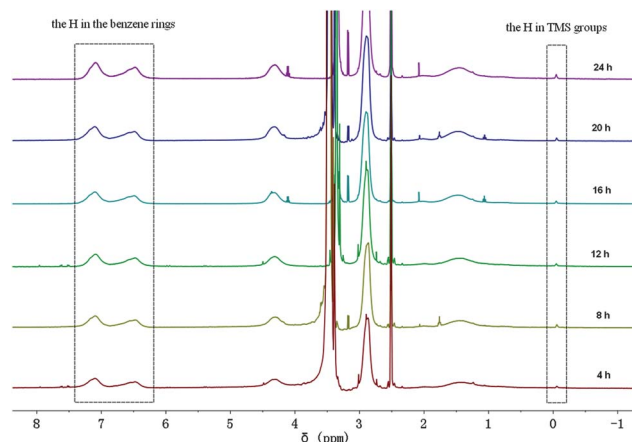

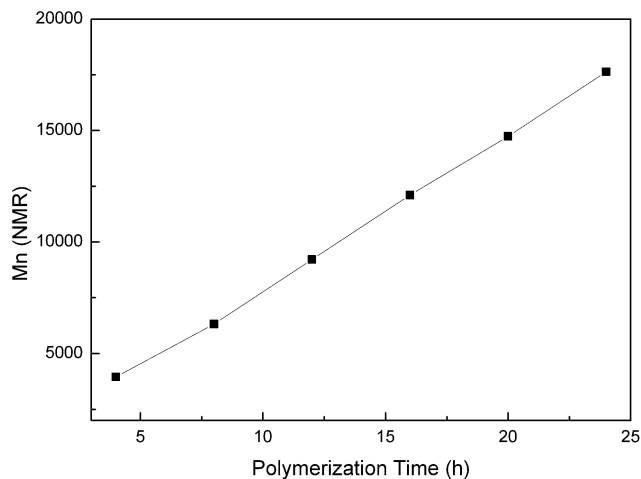Fig. 5 ^{1}H NMR spectra of the TMS-P[VBTMA][BF$_4$] at different polymerization times.

Fig. 6 Plot of M_n of TMS-P[VBTMA][BF$_4$] obtained from ^{1}H NMR.

worked for some charged polymers[53,54] and quaternary ammonium salts can take advantage of their inherent matrix suppression effect (MSE) and analyte suppression effect (ASE),[55] no peak was observed for P[VBTMA][BF$_4$] by MALDI-TOF MS under many tested conditions with different matrices. Overall, the MW and MWD characterization of poly(ionic liquid)s is still a challenging issue that must be solved.

3.3 Thermal properties

Thermogravimetric curves of the silica particles, SiO$_2$–Br, and SiO$_2$–P[VBTMA][BF$_4$] (with a polymerization time of 16 h) are shown in Fig. 7. Compared with the TGA diagram of the nanosilica particles, the much higher weight loss observed in the TGA diagram of SiO$_2$–Br and SiO$_2$–P[VBTMA][BF$_4$] originates from the organic composition of the composites. Before thermal decomposition a slight weight loss of around 2.2%, as shown in Fig. 7(b), is probably due to the evaporation of physically absorbed moisture, and this value is a little higher in the
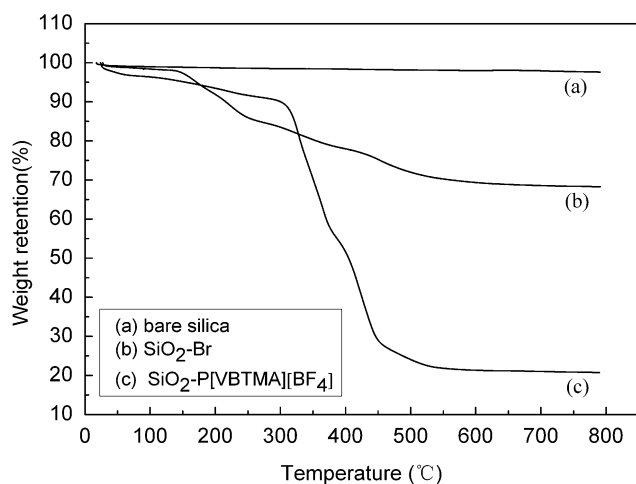
P[VBTMA][BF$_4$]-grafted composite particles, which is caused by the high hydrophilicity of the P[VBTMA][BF$_4$] shell. SiO$_2$–Br clearly shows two types of distinct weight loss events: successive rapid decompositions at 140 °C and 260 °C due to the decomposition of the organic shell *vs.* the relatively slow weight loss region at around 520–700 °C due to the intermolecular condensation of the silica particles. The weight retention obtained for SiO$_2$–P[VBTMA][BF$_4$] (Fig. 7(c)) at 750 °C is only 20.8%. Using the weight retention at 750 °C obtained for SiO$_2$–Br (68.4%) as a reference, the P[MATMA][BF$_4$] weight content is calculated to be 47.6%. Two rapid thermal degradation events of SiO$_2$–P[VBTMA][BF$_4$] occur at 305 °C and 395 °C under a N$_2$ atmosphere, which are due to the cleavage of the P[VBTMA][BF$_4$] polymer backbone (or the so-called carbonation). The high decomposition temperature of SiO$_2$–P[VBTMA][BF$_4$] (over 300 °C) indicated its excellent thermal stability. Apparently, the present nanocomposite polyelectrolyte is fairly stable below 300 °C, making it resistant to high temperature under continuous irradiation or other tough conditions.

3.4 Morphology of the silica nanoparticles grafted with the P[VBTMA][BF$_4$] shell

The SEM images shown in Fig. 8 demonstrate the morphology and dispersion of bare silica, SiO$_2$–Br, SiO$_2$–P[VBTMA][BF$_4$], and P[VBTMA][BF$_4$] with a polymerization time of 16 h. The remarkable difference between the dispersion states of SiO$_2$ particles, SiO$_2$–Br particles and SiO$_2$–P[VBTMA][BF$_4$] particles (with a polymerization time of 16 h) can be easily recognized. The slight increase in particle size can also be recognized. In Fig. 8(a), the high tendency to form aggregates is due to the high surface energy of the SiO$_2$ particles. Compared with the dispersion of silica particles without surface treatment, SiO$_2$–Br particles (Fig. 8(b)) show better dispersity with a little larger particle size. Due to the grafted polymer, the particles with the P[VBTMA][BF$_4$] shell (Fig. 8(c)) show a slight increase in particle size. There is also a much less tendency to form larger aggregates than the SiO$_2$–Br particles. This can be attributed to the high hydrophilicity of the P[VBTMA][BF$_4$] shell and appears to
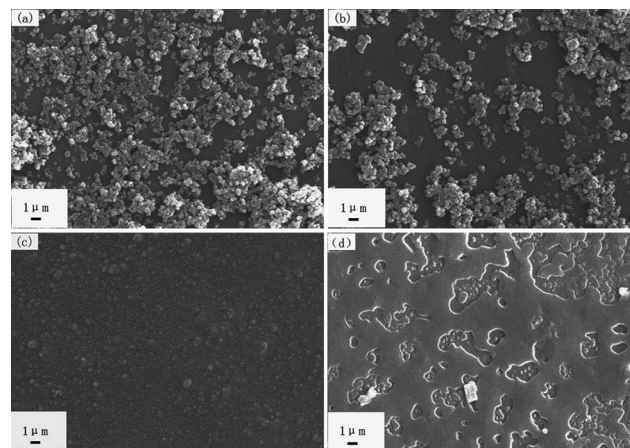

Fig. 7 TGA diagrams of (a) bare silica, (b) SiO$_2$–Br and (c) SiO$_2$–P[VBTMA][BF$_4$].

Fig. 8 SEM images of (a) bare silica, (b) SiO$_2$–Br, (c) SiO$_2$–P[VBTMA]-[BF$_4$], and (d) P[VBTMA][BF$_4$].

depend strongly on the amorphous character of P[VBTMA]-[BF$_4$].[56] As a result, highly dispersed membranes tend to be formed. As shown in Fig. 8(d), a laminated structure with a smooth surface is formed by pure poly(ionic liquid)s, while in Fig. 8(c), a membrane is formed by the nanocomposites. Many aggregations of nanoparticles are distributed on the membrane, offsetting the blanks in the polymers.

On the other hand, the dispersion property of SiO$_2$–P-[VBTMA][BF$_4$] became better as the polymerization time prolonged (the SEM images are shown in Fig. S2†). A tentative inference on this result is that the percolation effect and aggregation effect of the nanoparticles decrease after the P[VBTMA][BF$_4$] shell is grafted onto the nanosilica. The grafting of P[VBTMA][BF$_4$] changes the dispersion of the nanoparticles. Therefore, the properties change.

3.5 Ionic conductivity measurement

Ionic conductivity of the pure polymer with a polymerization time of 16 h and that of the grafted nanocomposites with different polymerization times are listed in Table 2. Since the cations of P[VBTMA][BF$_4$] are immobilized on polymer chains, their migration is negligible and only the anions retain high mobility. Therefore, P[VBTMA][BF$_4$] exhibits pure anionic conductivity.
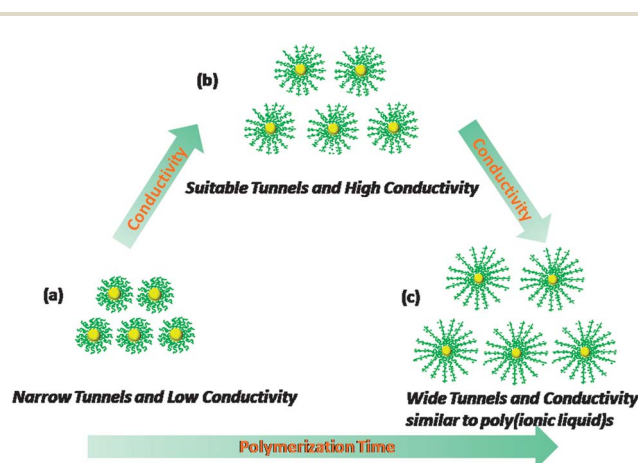
The effect of the composition of nanoparticles on the ionic conductivity was also investigated. It has been demonstrated that the addition of inorganic nanoparticles such as SiO$_2$ and TiO$_2$ can increase the ionic conductivity of the low-fluidity solid electrolyte.[22–26] As shown in Table 2, the ionic conductivity of SiO$_2$–P[VBTMA][BF$_4$] far exceeds that of the pure polymer P[VBTMA][BF$_4$] with the same polymerization time (e.g. 16 h). Furthermore, the hybrid nanomaterials of SiO$_2$–P[VBTMA][BF$_4$] with different contents of grafted P[VBTMA][BF$_4$] have higher ionic conductivity than the pure polymer P[VBTMA][BF$_4$] with a polymerization time of 16 h. The ionic conductivity of nanocomposites increases to a maximum prior to decreasing as the polymerization time prolongs. For nanosilica, the ionic conductivity is only 0.40 μS cm^{-1}. At the beginning, though the graft density of P[VBTMA][BF$_4$] on the surface is low, the ionic conductivity of the hybrid nanomaterial is not only much higher than that of pure nanosilica, but also a little higher than that of the pure polymer. It is because of the highly conductive layer formed at the polymer–silica interface. As the polymerization time is prolonged, P[VBTMA][BF$_4$] grafted on the silica surface

increases, the free ion number increases, and the ionic channel becomes wider, thus leading to a higher ionic conductivity. However, after a polymerization time of 16 h, with a degree of polymerization (DP) of 45 and a MW of 12 106 g mol^{-1} of the P[VBTMA][BF$_4$] shell (according to ^{1}H NMR analysis shown in Fig. 6) and the P[VBTMA][BF$_4$] content of 47.6% (according to TGA analysis), the ionic conductivity of the nanocomposites decreases with further increase of the grafted P[VBTMA][BF$_4$]. We attribute this phenomenon to the limited contact surface region of the silica core (Scheme 1). After a certain polymerization time, the fraction of the highly conductive layer decreases as the grafted P[VBTMA][BF$_4$] shell increases, leading to the decreased ionic conductivity of the nanocomposites. This effect is likely due to a combination of the formation of the highly conductive layer and the increase in the number of charge carriers inside the conducting phase. A possible process of the change of ionic conductivity is proposed as follows according to their composition.

The structure of the nanocomposite polyelectrolyte is schematically presented in Scheme 2. The nitrogen atoms in the polymer can interact with the hydroxyl groups on the nanoparticle surface, which can be supported by the IR analysis results (Fig. 1). Compared with Fig. 1(a), the band related to hydroxyl groups of silica in Fig. 1(c) shifts from 3435 to 3428 cm^{-1}, which is caused by the hydrogen bonds formed between hydroxyl groups on silica particles and nitrogen atoms in the polymer. Thus, as shown in Scheme 2(a), a high ion density layer is formed around the silica particles. After a certain polymerization time, as the grafted P[VBTMA][BF$_4$] chain becomes longer, the percolation effect and aggregation effect of the nanoparticles weaken, leading to wider channels for ion conduction (Scheme 2(b)). After a polymerization time of 16 h, the content of nanosilica becomes too small (as shown in Scheme 2(c)) so that the increase in ionic conductivity of the nanocomposites is no longer evident, but the ionic conductivity is still higher than that of pure polymers. This also confirms that the addition of an adequate amount of inorganic nanoparticles can improve the ionic conductivity of the polymer electrolytes.

Table 2 Ionic conductivity of pure nanosilica, P[VBTMA][BF$_4$] and SiO$_2$–P[VBTMA][BF$_4$] with different polymerization times

No.	Sample name	Polymerization time (h)	Conductivity (μS cm^{-1})
1	SiO$_2$	0	0.40
2	SiO$_2$–P[VBTMA][BF$_4$]-1	4	32.8
3	SiO$_2$–P[VBTMA][BF$_4$]-2	8	74.2
4	SiO$_2$–P[VBTMA][BF$_4$]-3	12	68.6
5	SiO$_2$–P[VBTMA][BF$_4$]-4	16	104
6	SiO$_2$–P[VBTMA][BF$_4$]-5	20	26.8
7	SiO$_2$–P[VBTMA][BF$_4$]-6	24	28.6
8	P[VBTMA][BF$_4$]	16	18.6

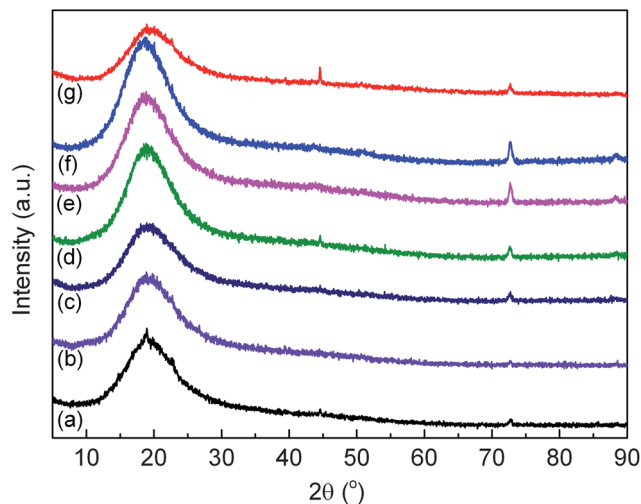**Scheme 2** Schematic of the arrangement structure of SiO$_2$–P-[VBTMA][BF$_4$] at different compositions.

Fig. 9 XRD patterns of poly(ionic liquid)s-based polyelectrolyte: (a) pure P[VBTMA][BF$_4$]; (b) SiO$_2$–P[VBTMA][BF$_4$]-1; (c) SiO$_2$–P[VBTMA]-[BF$_4$]-2; (d) SiO$_2$–P[VBTMA][BF$_4$]-3; (e) SiO$_2$–P[VBTMA][BF$_4$]-4; (f) SiO$_2$–P[VBTMA][BF$_4$]-5; (g) SiO$_2$–P[VBTMA][BF$_4$]-6.

As is well-known, the crystallinity of polyelectrolytes has a significant effect on their ionic conductivity;[22] therefore, X-ray diffraction measurement was performed to examine the crystallinity of pure P[VBTMA][BF$_4$] with a polymerization time of 16 h and the SiO$_2$–P[VBTMA][BF$_4$] nanocomposites of different polymerization times. The XRD curves are shown in Fig. 9. Pure P[VBTMA][BF$_4$] exhibits a broad peak at a 2θ angle of 12°–27°. From curve (a) to curve (b), the large diffraction peak intensity of XRD for the SiO$_2$–P[VBTMA][BF$_4$] composites was slightly reduced after P[VBTMA][BF$_4$] was grafted onto the nanosilica, which destroyed the crystalline part of P[VBTMA][BF$_4$] and reduced the crystallinity of P[VBTMA][BF$_4$]. What is more, when the content of the nanosilica core decreased from curve (b) to curve (f), the relative intensity of the crystallization peaks further increased. The crystallinity of nanocomposites calculated from the XRD peaks for curve (b–g) is 0.49, 0.56, 0.73, 0.83, 0.87, and 1.52. This is attributed to the fact that some crystal defects and free volume appear at the interface of inorganic particles and the polymer after nanosilica is introduced into the conducting system. Hence, the crystallinity of P[VBTMA][BF$_4$] increased and the proportion of the amorphous region decreased as the content of nanosilica decreased. There is significant motion of anions and even polymer chains in the amorphous phase and the free volume at the interface between P[VBTMA][BF$_4$] and the silica core. The amorphous phase increases while the free volume decreases with the increase of the nanosilica content, thereby the change of ionic conductivity of SiO$_2$–P[VBTMA][BF$_4$] composites should be a cumulative result of the increasing amorphous phase region and the decreasing free volume. Through our experiments, we found that the optimal ionic conductivity was obtained from the nanocomposite with a polymerization time of 16 h.

Based on the above discussion, the highest ionic conductivity value ($\sigma = 104$ μS cm^{-1}, in the order of 10^{-4} S cm^{-1}) of the nanocomposites at room temperature is probably due to the formation of a highly conductive layer and high-efficiency ion

migration tunnels at the polymer–silica interface. The hydrogen bond interactions make the grafted P[VBTMA][BF$_4$] arrange around the SiO$_2$ nanoparticles closely and densely, which is very important to form the highly conductive layer. As a result, high-efficiency ion migration tunnels with mechanical stability are constructed, which is beneficial to the improvement of conductivity as mentioned above. As a whole, the interfacial resistance of this organic–inorganic nanocomposite polyelectrolyte influences the total resistance of the nanomaterial significantly and so does the crystallinity of the nanocomposite.

3.6 Ion-conducting behavior

It has been shown that at room temperature the optimal SiO$_2$–P[VBTMA][BF$_4$] nanocomposite electrolyte (with a polymerization time of 16 h, DP of 45 and MW of 12 106 g mol^{-1} of the P[VBTMA][BF$_4$] shell, and the P[VBTMA][BF$_4$] content of 47.6%) has the highest ionic conductivity. The temperature dependence of ionic conductivity was also measured to further characterize the ionic conductivity properties of the electrolytes (Fig. 10). Both P[VBTMA][BF$_4$] and SiO$_2$–P[VBTMA][BF$_4$] exhibit an exponential increase of ionic conductivity with temperature over a limited temperature range (303.15–353.15 K), which is consistent with Arrhenius behavior. In fact, the data in Fig. 10 can be fitted well by the following Arrhenius equation (eq (4)):

$$\sigma(T) = A\exp\left(\frac{-E_a}{RT}\right) \tag{4}$$

where A is a constant, E_a is the activation energy, R is the gas constant ($=8.314$ J mol^{-1} K^{-1}), and T is the absolute temperature.

The E_a of the pure P[VBTMA][BF$_4$] electrolyte (Fig. 10(b)) is calculated to be 32.33 kJ mol^{-1}. Such a high value indicates inferior ionic conduction.[27,57] As for the nanocomposite with silica nanoparticles (Fig. 10(a)), the E_a is obviously reduced (15.08 kJ mol^{-1}), because of the formation of high-efficiency ion exchange tunnels by introducing SiO$_2$. This lower value is even
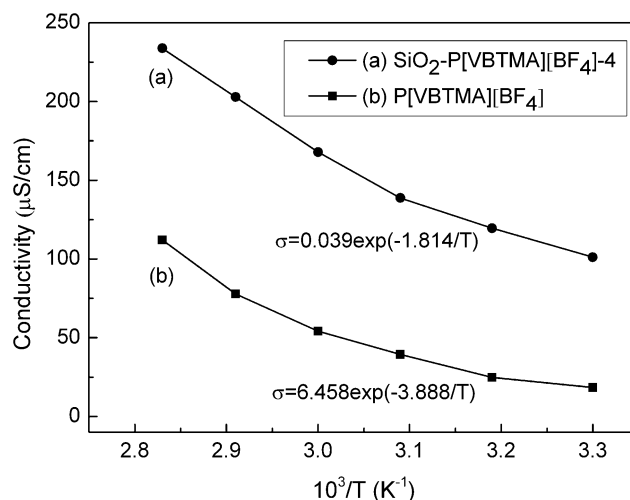

Fig. 10 Temperature dependence of ionic conductivity of (a) SiO$_2$–P[VBTMA][BF$_4$]-4 and (b) P[VBTMA][BF$_4$].

comparable to the reported data of gel electrolytes for quasi-solid-state dye-sensitized solar cells[57] and thus may meet the requirement of their practical application in many fields.

4. Conclusion

In summary, a kind of novel core–shell P[VBTMA][BF$_4$]-based solid-state nanocomposite polyelectrolyte using rigid inorganic nanosilica as the core has been fabricated and was confirmed by FT-IR, ^{1}H NMR and XPS. The molecular weight of the polymer that was grafted onto the nanosilica was measured with a TMS-labeled "sacrificial initiator" method by ^{1}H NMR. TGA curves indicate good thermal stability of the nanocomposites. SEM images show their uniform and spherical morphology and dispersion information. By optimization of the composition (with a polymerization time of 16 h and the P[VBTMA][BF$_4$] content of 47.6%) of the electrolyte, considerable ionic conductivity above 10^{-4} S cm^{-1} is achieved at room temperature.

In addition, the enhancement of conductivity is related to the combination of the formation of a highly conductive layer and a decrease in crystallinity of P[VBTMA][BF$_4$] according to the XRD result. Besides, the conductivity–temperature behaviors can be fitted well by the Arrhenius equation and it shows a lower activation energy (15.08 kJ mol^{-1}) than pure P[VBTMA]-[BF$_4$].

Overall, the tunable ionic conductivity was achieved by varying over the composition *via* changing the chain length of the grafted polymer and the size of the nanosilica particles. Also, due to the versatile applicability of SI-ATRP, the resulting ion-conducting nanocomposites are promising for applications that require moderate ion conduction.

Acknowledgements

References

1 A. S. Shaplov, E. I. Lozinskaya, R. Losada, C. Wandrey, A. T. Zdvizhkov, A. A. Korlyukov, K. A. Lyssenko, I. A. Malyshkina and Y. S. Vygodskii, *Polym. Adv. Technol.*, 2011, **22**, 448–457.

2 B. Yameen, A. Kaltbeitzel, G. Glasser, A. Langner, F. Müller, U. Gösele, W. Knoll and O. Azzaroni, *ACS Appl. Mater. Interfaces*, 2010, **2**, 279–287.

3 J. Y. Yuan and M. Antonietti, *Polymer*, 2011, **52**, 1469–1482.

4 D. Mecerreyes, *Prog. Polym. Sci.*, 2011, **36**, 1629–1648.

5 B. Yu, F. Zhou, C. W. Wang and W. M. Liu, *Eur. Polym. J.*, 2007, **43**, 2699–2707.

6 K. Matsumoto and T. Endo, *Macromolecules*, 2009, **42**, 4580–4584.

7 C. C. Yang, *J. Membr. Sci.*, 2007, **288**, 51–60.

8 A. Lewandowski and A. Świderska, *Solid State Ionics*, 2004, **169**, 21–24.

9 S. Fotiadou, C. Karageorgaki, K. Chrissopoulou, K. Karatasos, I. Tanis, D. Tragoudaras, B. Frick and S. H. Anastasiadis, *Macromolecules*, 2013, **46**, 2842–2855.

10 Y. Schneider, M. A. Modestino, B. L. McCulloch, M. L. Hoarfrost, R. W. Hess and R. A. Segalman, *Macromolecules*, 2013, **46**, 1543–1548.

11 J. W. Zhang, X. B. Huang, H. Wei, J. W. Fu, Y. W. Huang and X. Z. Tang, *J. Solid State Electrochem.*, 2012, **16**, 101–107.

12 G. X. Wang, L. Sun, D. H. Bradhurst, S. Zhong, S. X. Dou and H. K. Liu, *J. Power Sources*, 2000, **88**, 278–281.

13 Y. Liu, J. Y. Lee and L. Hong, *J. Appl. Polym. Sci.*, 2003, **89**, 2815–2822.

14 R. C. B. Scaravelli, R. L. Dazzi, F. C. Giacomelli, G. Machado, C. Giacomelli and V. Schmidt, *J. Colloid Interface Sci.*, 2013, **397**, 114–121.

15 Z. B. Li, T. Y. Chen, J. J. Nie, J. T. Xu, Z. Q. Fan and B. Y. Du, *Mater. Chem. Phys.*, 2013, **138**, 650–657.

16 S. Coe-Sullivan, W.-K. Woo, J. S. Steckel, M. Bawendi and V. Bulović, *Org. Electron.*, 2003, **4**, 123–130.

17 L. Lukyanova, L. Séon, A. Aradian, O. Mondain-Monval, J. Leng and R. Wunenburger, *J. Appl. Polym. Sci.*, 2013, **128**, 3512–3521.

18 C. Sanchez, B. Julián, P. Belleville and M. Popall, *J. Mater. Chem.*, 2005, **15**, 3559–3592.

19 J. T. Yang, Y. Sang, F. Chen, Z. D. Fei and M. Q. Zhong, *J. Supercrit. Fluids*, 2012, **62**, 197–203.

20 H. J. Yu and Z. H. Luo, *J. Polym. Sci., Part A: Polym. Chem.*, 2010, **48**, 5570–5580.

21 F. Hoffmann, M. Cornelius, J. Morell and M. Fröba, *Angew. Chem., Int. Ed.*, 2006, **45**, 3216–3251.

22 D. R. MacFarlane, P. J. Newman, K. M. Nairn and M. Forsyth, *Electrochim. Acta*, 1998, **43**, 1333–1337.

23 J.-W. Kim, K.-S. Ji, J.-P. Lee and J.-W. Park, *J. Power Sources*, 2003, **119–121**, 415–421.

24 A. Walcarius, C. Delacote and S. Sayen, *Electrochim. Acta*, 2004, **49**, 3775–3783.

25 D. Fu, B. Luan, S. Argue, M. N. Bureau and I. J. Davidson, *J. Power Sources*, 2012, **206**, 325–333.

26 H. X. Wang, H. Li, B. F. Xue, Z. X. Wang, Q. B. Meng and L. Q. Chen, *J. Am. Chem. Soc.*, 2005, **127**, 6394–6401.

27 J. F. Shi, L. Wang, Y. L. Liang, S. J. Peng, F. Y. Cheng and J. Chen, *J. Phys. Chem. C*, 2010, **114**, 6814–6821.

28 X. Y. He, W. Yang and X. W. Pei, *Macromolecules*, 2008, **41**, 4615–4621.

29 W. P. Wang, H. M. Cao, G. J. Zhu and P. Wang, *J. Polym. Sci., Part A: Polym. Chem.*, 2010, **48**, 1782–1790.

30 T. Werne and T. E. Patten, *J. Am. Chem. Soc.*, 2001, **123**, 7497–7505.

31 H. D. Tang, J. B. Tang, S. J. Ding, M. Radosz and Y. Q. Shen, *J. Polym. Sci., Part A: Polym. Chem.*, 2005, **43**, 1432–1443.

32 A. Carlmark and E. Malmström, *J. Am. Chem. Soc.*, 2002, **124**, 900–901.

33 W. H. Yu, E. T. Kang, S. P. Zhu and K. G. Neoh, *J. Phys. Chem. B*, 2003, **107**, 10198–10205.

34 W. Feng, S. P. Zhu, K. Ishihara and J. L. Brash, *Langmuir*, 2005, **21**, 5980–5987.

35 K. Ohno, T. Morinaga, K. Koh, Y. Tsujii and T. Fukuda, *Macromolecules*, 2005, **38**, 2137–2142.

36 R. E. Behling, B. A. Williams, B. L. Staade, L. M. Wolf and E. W. Cochran, *Macromolecules*, 2009, **42**, 1867–1872.

37 A. A. Brown, N. S. Khan, L. Steinbock and W. T. S. Huck, *Eur. Polym. J.*, 2005, **41**, 1757–1765.

38 S. Edmondson, C.-D. Vo and S. P. Armes, *Macromolecules*, 2007, **40**, 5271–5278.

39 S. Edmondson, C.-D. Vo and S. P. Armes, *Langmuir*, 2008, **24**, 7208–7215.

40 S. Edmondson, N. T. Nguyen, A. L. Lewis and S. P. Armes, *Langmuir*, 2010, **26**, 7216–7226.

41 Y. Q. Shen, S. P. Zhu and R. Pelton, *Macromolecules*, 2001, **34**, 5812–5818.

42 J. F. Moll, P. Akcora, A. Rungta, S. S. Gong, R. H. Colby, B. C. Benicewicz and S. K. Kumar, *Macromolecules*, 2011, **44**, 7473–7477.

43 D. Dukes, Y. Li, S. Lewis, B. Benicewicz, L. Schadler and S. K. Kumar, *Macromolecules*, 2010, **43**, 1564–1570.

44 D. Maillard, S. K. Kumar, B. Fragneaud, J. W. Kysar, A. Rungta, B. C. Benicewicz, H. Deng, L. C. Brinson and J. F. Douglas, *Nano Lett.*, 2012, **12**, 3909–3914.

45 A. Rungta, B. Natarajan, T. Neely, D. Dukes, L. S. Schadler and B. C. Benicewicz, *Macromolecules*, 2012, **45**, 9303–9311.

46 T. Werne and T. E. Patten, *J. Am. Chem. Soc.*, 1999, **121**, 7409–7410.

47 A. Carlmark and E. E. Malmström, *Biomacromolecules*, 2003, **4**, 1740–1745.

48 G. Morandi, L. Heath and W. Thielemans, *Langmuir*, 2009, **25**, 8280–8286.

49 K. Ohno, K.-M. Koh, Y. Tsujii and T. Fukuda, *Macromolecules*, 2002, **35**, 8989–8993.

50 H. K. He, M. J. Zhong, B. Adzima, D. Luebke, H. Nulwala and K. Matyjaszewski, *J. Am. Chem. Soc.*, 2013, **135**, 4227–4230.

51 M. Päch, D. Zehm, M. Lange, I. Dambowsky, J. Weiss and A. Laschewsky, *J. Am. Chem. Soc.*, 2010, **132**, 8757–8765.

52 Y. N. Zhou and Z. H. Luo, *Polym. Chem.*, 2013, **4**, 76–84.

53 B. Dervaux, F. Meyer, J.-M. Raquez, A. Olivier, F. E. D. Prez and P. Dubois, *Macromol. Chem. Phys.*, 2012, **213**, 1259–1265.

54 T. Biedroń and P. Kubisa, *J. Polym. Sci., Part A: Polym. Chem.*, 2008, **46**, 6961–6968.

55 X. W. Lou, J. L. J. Dongen, J. A. J. M. Vekemans and E. W. Meijer, *Rapid Commun. Mass Spectrom.*, 2009, **23**, 3077–3082.

56 J. B. Tang, H. D. Tang, W. L. Sun, M. Radosz and Y. Q. Shen, *Polymer*, 2005, **46**, 12460–12467.

57 J. F. Shi, S. J. Peng, J. Pei, Y. L. Liang, F. Y. Cheng and J. Chen, *ACS Appl. Mater. Interfaces*, 2009, **1**, 944–950.